Identifying sensitive areas of adaptive observations for prediction of the Kuroshio large meander using a shallow-water model*

ZOU Guang'an (邹广安)[1, 2, 3], WANG Qiang (王强)[1, **], MU Mu (穆穆)[1]

[1] Key Laboratory of Ocean Circulation and Waves, Institute of Oceanology, Chinese Academy of Sciences, Qingdao 266071, China

[2] University of Chinese Academy of Sciences, Beijing 100049, China

[3] School of Mathematics and Statistics, Henan University, Kaifeng 475004, China

Abstract   Sensitive areas for prediction of the Kuroshio large meander using a 1.5-layer, shallow-water ocean model were investigated using the conditional nonlinear optimal perturbation (CNOP) and first singular vector (FSV) methods. A series of sensitivity experiments were designed to test the sensitivity of sensitive areas within the numerical model. The following results were obtained: (1) the effect of initial CNOP and FSV patterns in their sensitive areas is greater than that of the same patterns in randomly selected areas, with the effect of the initial CNOP patterns in CNOP sensitive areas being the greatest; (2) both CNOP- and FSV-type initial errors grow more quickly than random errors; (3) the effect of random errors superimposed on the sensitive areas is greater than that of random errors introduced into randomly selected areas, and initial errors in the CNOP sensitive areas have greater effects on final forecasts. These results reveal that the sensitive areas determined using the CNOP are more sensitive than those of FSV and other randomly selected areas. In addition, ideal hindcasting experiments were conducted to examine the validity of the sensitive areas. The results indicate that reduction (or elimination) of CNOP-type errors in CNOP sensitive areas at the initial time has a greater forecast benefit than the reduction (or elimination) of FSV-type errors in FSV sensitive areas. These results suggest that the CNOP method is suitable for determining sensitive areas in the prediction of the Kuroshio large-meander path.

Keyword: Kuroshio large meander; conditional nonlinear optimal perturbation (CNOP); first singular vector (FSV); sensitive areas

1 INTRODUCTION

The Kuroshio is the western boundary current of the wind-driven subtropical gyre in the North Pacific Ocean. The Kuroshio path south of Japan has remarkable bimodal features comprising large meander (LM) and non-large meander (NLM) paths (Taft, 1972; Kawabe, 1995). Changes between these two kinds of paths have profound effects on the climate and marine environment of the western North Pacific region. It is thus important to study the prediction of Kuroshio path variations.

In recent years, researchers have focused on the effects of initial errors on prediction results, finding that the initial states affect the predictability of Kuroshio meander (Ishikawa et al., 2004; Miyazawa et al., 2005; Fujii et al., 2008; Wang et al., 2012). Therefore, the forecasting of a Kuroshio LM event may be improved by reducing initial uncertainties in ocean forecasts. The accuracy of the initial condition can be enhanced through ocean observations. However, it is too expensive and difficult to make observations over the entire ocean, and targeted observation techniques (i.e., adaptive observations)

have thus been attempted.

The aim of adaptive observations is to improve forecast results by implementing an observation network in specific regions, where additional observations are expected to reduce the forecast errors. These regions may be considered "sensitive areas" where improvements to the initial conditions are anticipated to have a greater forecast benefits than improvements in other areas (Langland, 2005; Mu et al., 2009).

Adaptive observations have been used to improve forecasts in various research fields, such as weather forecasting (Berliner et al., 1999; Morss et al., 2001) and the prediction of tropical cyclones (Bishop et al., 2001; Hamill and Snyder, 2002; Majumdar et al., 2006; Mu et al., 2009; Qin and Mu, 2011) and the El Niño Southern Oscillation (Yu et al., 2012).

An important aspect of adaptive observations is determination of the sensitive areas. Strategies and approaches have been proposed to identify those areas for the adaptive observations. These approaches include the singular vector (Palmer et al., 1998; Bergot et al., 1999; Buizza and Montani, 1999), quasi-inverse (Pu et al., 1997; Pu and Kalnay, 1999), sensitivity vector (Langland and Rohaly, 1996), adjoint sensitivity (Baker and Daley, 2000), ensemble transform (Bishop and Toth, 1999), ensemble Kalman filter (Hamill and Snyder, 2002), and ensemble transform Kalman filter (Bishop et al., 2001). Mu et al. (2007) applied the conditional nonlinear optimal perturbation (CNOP) approach to study adaptive observations. The CNOP is a natural extension of the linear singular vector method into the nonlinear regime, and can represent initial errors that have the greatest nonlinear evolution (Mu et al., 2003; Mu, 2013). Furthermore, Mu et al. (2009) used CNOP to determine the sensitive areas for tropical cyclone predictions and compared the results with those from the first singular vector (FSV) method. The authors showed that CNOP-type errors have a greater effect than FSV-type errors on the forecast of a tropical cyclone.

The CNOP method was also used by Wang et al. (2013a) to investigate targeted observations for the prediction of Kuroshio path variations. However, further investigation is needed. For instance, Wang et al. used the "truth" field as the basic state with which to calculate the CNOP. However, we cannot know the true state of the ocean in a realistic prediction. In addition, the authors did not compare with any other approaches (such as the FSV) for the determination of

sensitive areas in adaptive observations. In this paper, the CNOP and FSV are used to study targeted observations for prediction of the Kuroshio LM, based on an analysis field obtained from control experiments. The sensitivity and validity of sensitive areas identified by these two methods are compared.

The remainder of the paper is as follows. Section 2 briefly describes the shallow-water ocean model and CNOP and FSV methods. Section 3 describes the two methods to identify sensitive areas for targeted observations, and examines the sensitivity and efficiencies of those areas. Section 4 presents a discussion and conclusions.

2 MODEL AND METHOD

2.1 Shallow-water ocean model

A 1.5-layer shallow-water ocean model was used to simulate Kuroshio path variations south of Japan. This model is similar to those used by Wang et al. (2012, 2013b). Here, we only give the essential description of the model. In spherical coordinates, the governing equations are

$$\frac{\partial u}{\partial t} + \frac{1}{r_0 \cos\theta}(u\frac{\partial u}{\partial\varphi} + v\cos\theta\frac{\partial u}{\partial\theta}) -$$

$$(f + \frac{u}{r_0}\tan\theta)v = \frac{-g'}{r_0\cos\theta}\frac{\partial h}{\partial\phi} +$$

$$A_h(\nabla^2 u - \frac{u}{r_0^2\cos^2\theta} - \frac{2\sin\theta}{r_0^2\cos^2\theta}\frac{\partial v}{\partial\phi}) +$$

$$\frac{\tau^\varphi}{\rho_0 h} - R_l u, \tag{1}$$

$$\frac{\partial v}{\partial t} + \frac{1}{r_0\cos\theta}(u\frac{\partial v}{\partial\varphi} + v\cos\theta\frac{\partial v}{\partial\theta}) +$$

$$(f + \frac{u}{r_0}\tan\theta)u = \frac{-g'}{r_0}\frac{\partial h}{\partial\theta} + A_h(\nabla^2 v -$$

$$\frac{v}{r_0^2\cos^2\theta} + \frac{2\sin\theta}{r_0^2\cos^2\theta}\frac{\partial u}{\partial\varphi}) + \frac{\tau^\theta}{\rho_0 h} - R_l v, \tag{2}$$

$$\frac{\partial h}{\partial t} + \frac{1}{r_0\cos\theta}[\frac{\partial}{\partial\varphi}(hu) + \frac{\partial}{\partial\theta}(hv\cos\theta)] = 0, \tag{3}$$

where (θ, φ) denotes the longitudinal and latitudinal coordinates, u and v are zonal and meridional velocities, respectively, and h is the upper-layer thickness with undisturbed value H=500 m. $f=2\Omega\sin\theta$ is the Coriolis parameter, $\Omega=7.292\times10^{-5}$/s is angular speed of the earth rotation of the earth, $r_0=6.37\times10^6$ m is the earth radius, g'=$g\Delta\rho/\rho_0$=0.044 m/
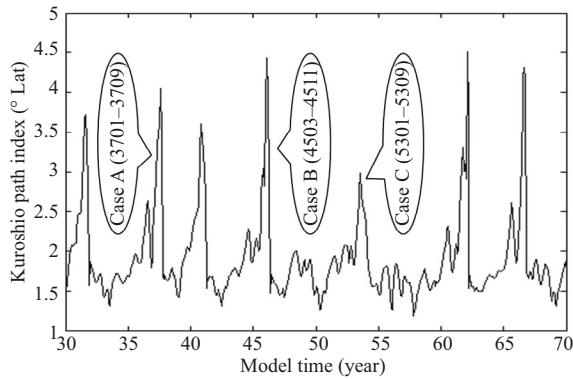
Fig.1 Time series of Kuroshio path index from 30 to 70 years of model time, where that index is defined as the mean value of the latitude difference between the Kuroshio axis (represented by the 520-m contour of the upper-layer thickness) and south coast of Japan between 136°E and 140°E

Three cases (A, B and C) were considered.

s^2 is reduced gravity, and τ^ϕ and τ^θ are zonal and meridional components of wind stress, respectively. The lateral friction coefficient is A_h=480 m^2/s, and the interfacial friction coefficient is R_I=4.5×10^{-8}/s.

The fully implicit Crank-Nicolson scheme is used to discretize the governing Eqs.1–3. The specific domain of the model covers the western North Pacific basin V: (15°–55°N, 122°E–158°W). The horizontal resolution is 0.2°×0.2°. A time step of 10 days was used. The flow was driven by the monthly climatological wind stress of Hellerman and Rosenstein (1983). The 200-m isobath was taken as the continental boundary to prevent the modeled Kuroshio from entering the East China Sea. No-slip boundary conditions were used in the model.

The model was integrated over 70 years. The results of the last 40 years were analyzed. The 520-m contour of the h in the model was taken as the Kuroshio axis. The Kuroshio path index was used to measure the state of the path, and was defined as the mean value of the latitude difference between the Kuroshio axis and south coast of Japan, within the longitude band 136°E to 140°E. According to this definition, the Kuroshio takes an LM path when the index is large; otherwise, it takes an NLM path. Figure 1 shows time series of the Kuroshio path indices. It is seen that the Kuroshio path has typical interannual variability and that the LM path occurred seven times in the 40 model years. The transition processes of Kuroshio paths in the seven cases appear similar. Snapshots of the upper-layer thickness field for three cases—A, B and C—are presented in this paper.

Taking Case B for example, the typical Kuroshio NLM path is shown in Fig.2a. A small meander in the Kuroshio path is evident in Fig.2b. The amplitude of this meander grows steadily (Fig.2c and d). In Fig.2e, the Kuroshio path develops into a significant LM state. That state is maintained for a period, but a cold-core eddy in the Kuroshio path is then shed (Fig.2f). Figure 2g shows that this isolated cold-core eddy detaches from the LM path and propagates westward. The Kuroshio path returns to an NLM state in Fig.2h. The simulation results of this model are similar to those in Fig.9 of Qiu and Miao (2000). The shallow-water model captures the essential features of the Kuroshio LM formation. Therefore, our model was used to study prediction of the Kuroshio LM path.

2.2 CNOP and FSV methods

In this subsection, we describe the CNOP and FSV methods for adaptive observations.

Let $X=(u, v, h)^T$ denote the state vector of the shallow-water model. The model can then be written as

$$X(t)=M_t(X_0), \tag{4}$$

where $X=(u_0, v_0, h_0)$ is the initial condition, M_t is the nonlinear propagator, and $X_t=(u_t, v_t, h_t)$ is the state vector at time t.

In this study, we explore the initial error that brings about the maximum prediction error. To find this error, we define a nonlinear constraint optimization problem:

$$J(x_{0\delta}) = \max_{\|x_0\|_a \leq \delta} J(x_0)$$
$$= \max_{\|x_0\|_a \leq \delta} \left\| M_t(X_0 + x_0) - M_t(X_0) \right\|_b^2, \tag{5}$$

where $J(x_0)=\|M_t(X_0+x_0)-M_t(X_0)\|_b^2$ is the objective function and $x_0=(u_0', v_0', h_0')$ denotes the initial error. $\|x_0\|_a \leq \delta$ is the initial constraint condition, with positive constraint radius δ.

To consider all possible factors affecting the prediction of the Kuroshio LM path, the constraint norm $\|\cdot\|_a^2$ is defined as the total energy of the initial error in the entire model domain V; therefore,

$$\|x_0\|_a^2 = \frac{1}{2}\{H\int_V [(u_0')^2 + (v_0')^2]dxdy +$$
$$g'\int_V (h_0')^2 dxdy\} \leq \delta^2. \tag{6}$$

The norm $\|\cdot\|_b^2$ for the objective function is defined as the kinetic energy of the initial error evolution at time t in the Kuroshio region south of Japan R (25°–
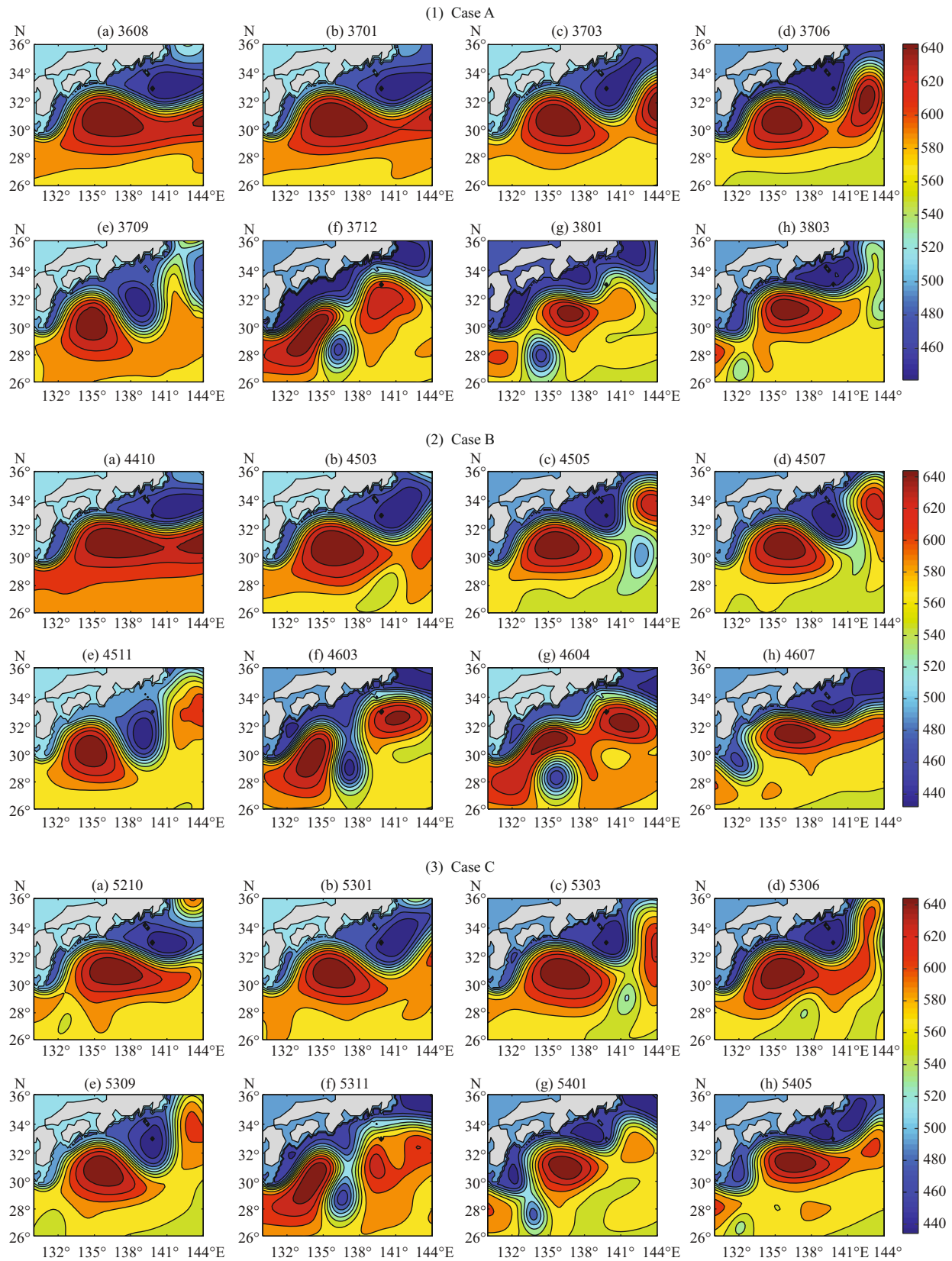
Fig.2 Snapshots of upper-layer thickness field, including LM events for (1) Case A (top, model years 36–38 approximately), (2) Case B (middle, model years 44–46 approximately), and (3) Case C (bottom, model years 52–54 approximately)

The numeral 3606 denotes model time of June in the 36th year. Unit is meters.

35°N, 132°–140°E), where the LM occurs. This norm can be written as

$$\left\| M_t(X_0 + x_0) - M_t(X_0) \right\|_b^2 = \left\| x(t) \right\|_b^2 =$$
$$\frac{1}{2} \int_R (h_t + h_t')[(u_t')^2 + (v_t')^2] \mathrm{d}x\mathrm{d}y, \tag{7}$$

where $x(t) = M_t(X_0 + x_0) - M_t(X_0) = (u_t', v_t', h_t')$ represents the nonlinear evolution of initial error x_0. This norm is chosen because the gradient of the objective function (Eq.7) is easy to obtain and the maximum can be efficiently obtained using the optimization algorithm. Additionally, this norm can clearly distinguish the different Kuroshio path states.

The solution $x_{0\delta}$ to problem (5) is called the CNOP. The CNOP is the initial error that leads to the maximum prediction error at prediction time t with the specific δ.

Suppose the initial error is sufficiently small and the time interval sufficiently short. Evolution of the initial error can then be approximately written as

$$M_t(X_0 + x_0) - M_t(X_0) \approx L_t|_{X0}(x_0), \tag{8}$$

where we call $L_t|_{X_0} = \partial M_t / \partial X_0$ the tangent linear version of the original nonlinear model, based on the initial reference state X_0. The FSV can be solved by considering the optimization problem

$$J(x_{0L}) = \max_{\|x_0\|_a^2 \neq 0} \frac{\left\| L_t|_{X_0}(x_0) \right\|_b^2}{\left\| x_0 \right\|_a^2}, \tag{9}$$

where norms $\|\cdot\|_a^2$ and $\|\cdot\|_b^2$ are defined the same as in the CNOP calculation.

The solution x_{0L} to problem (9) is called the FSV. The FSV represents fast-growing initial error in the tangent linear version of the originally nonlinear shallow-water model. Both the CNOP and FSV can be obtained using the spectral projected gradient 2 (SPG2) algorithm (Birgin et al., 2000).

3 RESULT

3.1 Sensitive areas

We investigated targeted observations for prediction of the Kuroshio LM path. Our aim was to determine the effects of the initial error on forecast results and forecasting improvements achieved by reducing that error, through making ocean observations. Therefore, transition processes from the NLM to LM path are taken as reference states, all of which start from the Kuroshio NLM state and end at the LM state at the final prediction time. We considered

the differences between sensitive areas for different types of Kuroshio LM events, such as events in which the strength of the Kuroshio LM and initial prediction time were different. Three cases (A, B and C) were chosen. Their path indices are shown in Fig.1 (where, for Case A, the numeral 3701 denotes a model target time of January in the 37th year, and 3709 designates a verification time of September in the same year). The LM path index in Case B is relatively large, whereas that in Case C is the smallest. Months of the initial prediction time in Cases A and C were the same, but differed from that of Case B. The transition process for Case B was similar to processes illustrated by Wang et al. (2012). Model outputs of the path from the NLM to LM were treated as the "truth". Optimization time intervals were 240 days in all three cases. The constraint radius was set as $\delta = 6.0 \times 10^5 \, \mathrm{m}^5/\mathrm{s}$, so that the amplitude of the upper-layer thickness component of the obtained initial perturbation was within 20 m.

We do not know the true ocean state at the future target time. We therefore superimposed the analysis errors onto the model two months before the target time and then integrated the model for 10 months. The outputs were treated as the analysis field. The analysis errors were obtained from the difference between two NLM path states at the target time in reference states before two LM events. This made the initial conditions as erroneous as possible for the control experiment, while keeping the dynamic balance between different model variables. Taking Case A as an example, we superimposed analysis errors at model time 3611 (November in the 36th year) and ran the model for 10 months, and we referred to the control run starting at the target time 3701 with analysis errors as a control experiment. This analysis field was used as the basic state in calculating the CNOP and FSV.

Figure 2 shows upper-layer thickness components of the CNOP and FSV (shaded) for each case. It is seen that large amplitudes of both the CNOP and FSV are mainly in the region of the Shikoku recirculation gyre (SRG) and south of the Kuroshio extension. In fact, upon calculating the CNOP and FSV in the seven LM cases, such large amplitudes were mainly in these two regions. As a matter of convenience, we only give results for three typical events (Cases A, B, and C). To compare the two types of perturbations, we superimposed the CNOP and FSV on the basic state and integrated the model to observe their effects on the forecast Kuroshio paths. Total energies of the
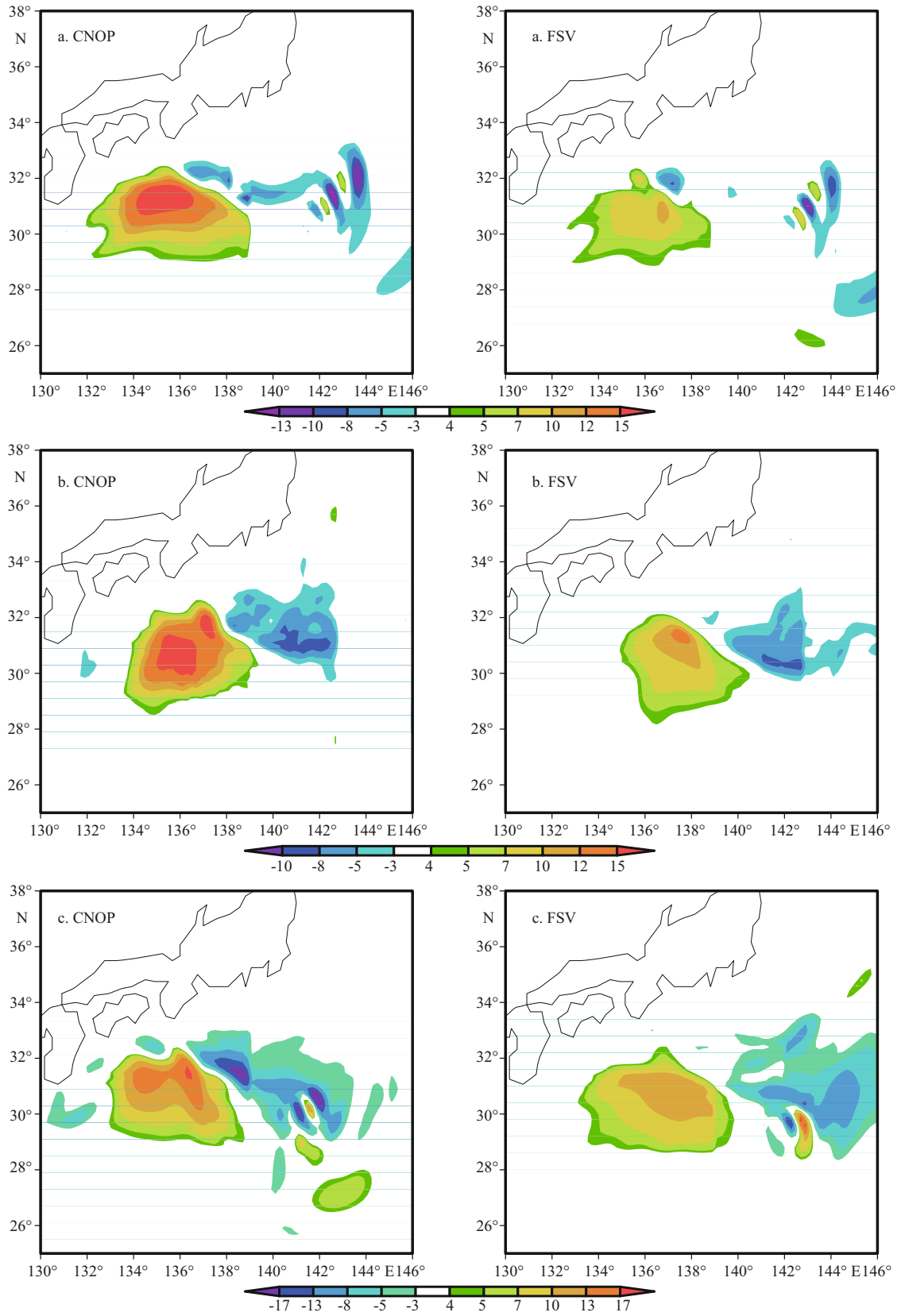
Fig.3 Upper-layer thickness components (shaded) of CNOP (left) and FSV (right) for (a) Case A, (b) Case B, and (c) Case C
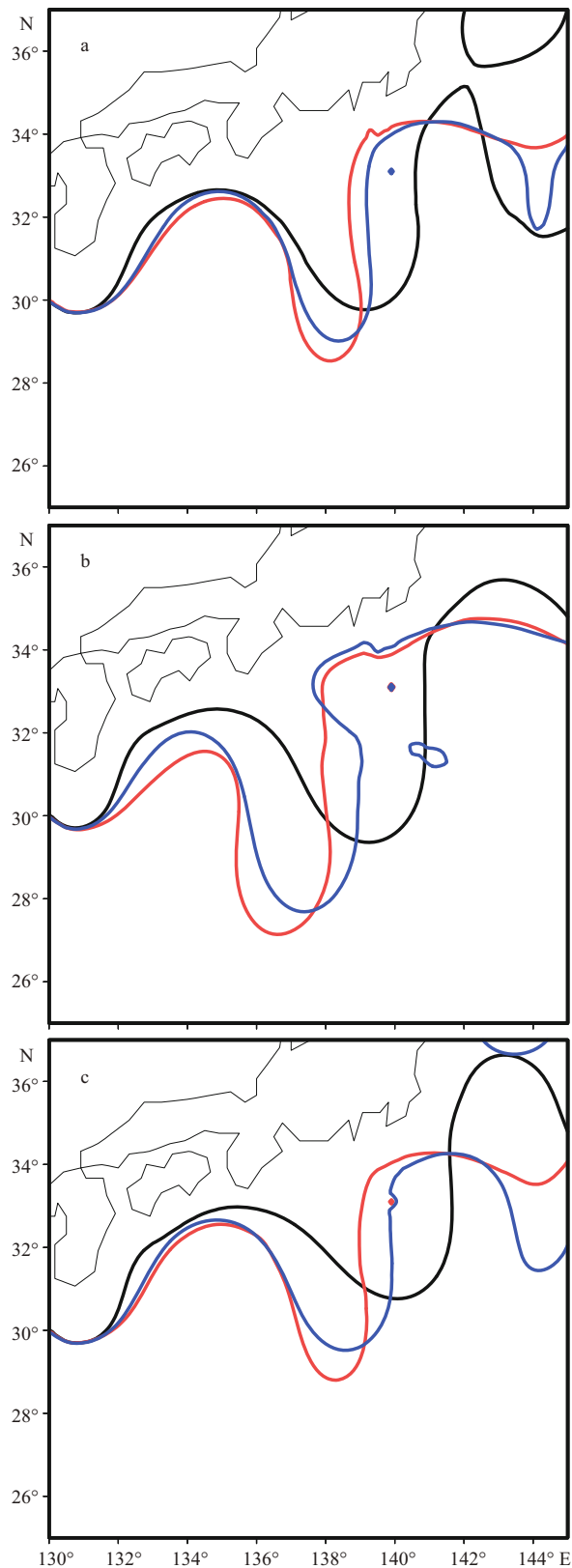
Unit for the thickness is meters.

Fig.4 Kuroshio axis (represented by 520-m contour of upper-layer thickness) for the basic states (black line) and flows perturbed by the CNOP (red line) and FSV (blue line) on day 240, for (a) Case A, (b) Case B, and (c) Case C

CNOP and FSV were identical throughout the simulation domain because δ was set to be the same in the CNOP and FSV calculations, and the CNOP and FSV solutions are always located at the boundary of the constraint condition. Figure 3 shows the Kuroshio axis generated on day 240 using the CNOP and FSV in the three cases. We see that both the CNOP and FSV strengthened the forecast Kuroshio LM paths, whereas the LM path generated with the FSV is weaker than that generated with the CNOP. Wang et al. (2012) demonstrated that the forecast Kuroshio LM is strengthened in a westward direction by the advection of momentum perturbations associated with nonlinear development of barotropic instabilities.

We now identify sensitive areas from the total energy distributions of the CNOP and FSV. Total energy (TE) at each grid point is calculated as

$$\|\cdot\|_{TE} = \frac{1}{2}(Hu_0'^2 + Hv_0'^2 + g'h_0'^2),\qquad(10)$$

where u_0', v_0', h_0' denotes the initial error.

Figures 4–6 show total energy distributions of the CNOP and FSV for each case. Areas with large amplitudes of total energies are in both the SRG region and south of the Kuroshio extension. Studies have shown that these two regions play an active role in the transition from a straight to meandering path (Ebuchi and Hanawa, 2000; Mitsudera et al., 2001; Ebuchi and Hanawa, 2003; Waseda et al., 2003; Tsujino et al., 2006; Wang et al., 2013a). Compared with the FSV results, the large CNOP amplitudes are toward the northwest. Here, grid points with large values of total energy distributions of the two initial perturbation types are defined as the sensitive areas, which are sorted by total energy in descending order. To compare the CNOP and FSV results, the same grid points (indicated by solid black dots (•) in Figs.5–7) were used; these areas are referred to as CNOP-SA and FSV-SA, respectively. The number of grid points in sensitive areas was chosen to be 154 in all three cases. Four randomly selected areas (R1, R2, R3, and R4) are shown in Fig.8. The numbers of grid points in these four areas are the same as those in the sensitive areas, and the center locations and zonal-meridional ratio of the grid points of randomly selected areas are the same in all three cases. In fact, regions R1 and R2 are not completely random selections. Previous studies have suggested that these are regions of major mesoscale fluctuation that are strongly related to the Kuroshio LM in the ocean general circulation model
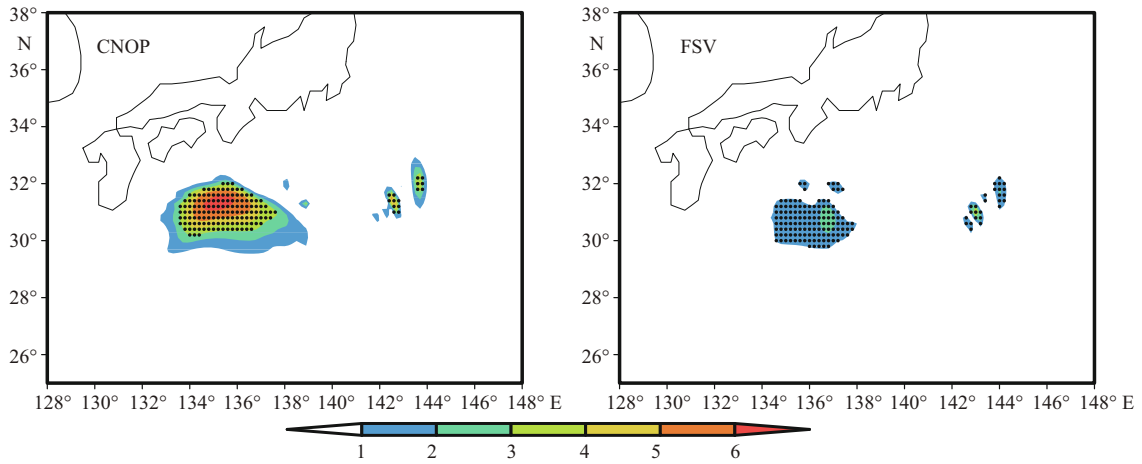
Fig.5 Total energy distributions (shaded) of CNOP (left) and FSV (right) for Case A

Units are m³/s². Regions marked by black solid dots (•) are treated as sensitive areas.

Fig.6 Total energy distributions (shaded) of CNOP (left) and FSV (right) for Case B

Units are m³/s². Regions marked by black solid dots (•) are treated as sensitive areas. The number of grid points is the same as in Case A.

Fig.7 Total energy distributions (shaded) of CNOP (left) and FSV (right) for Case C

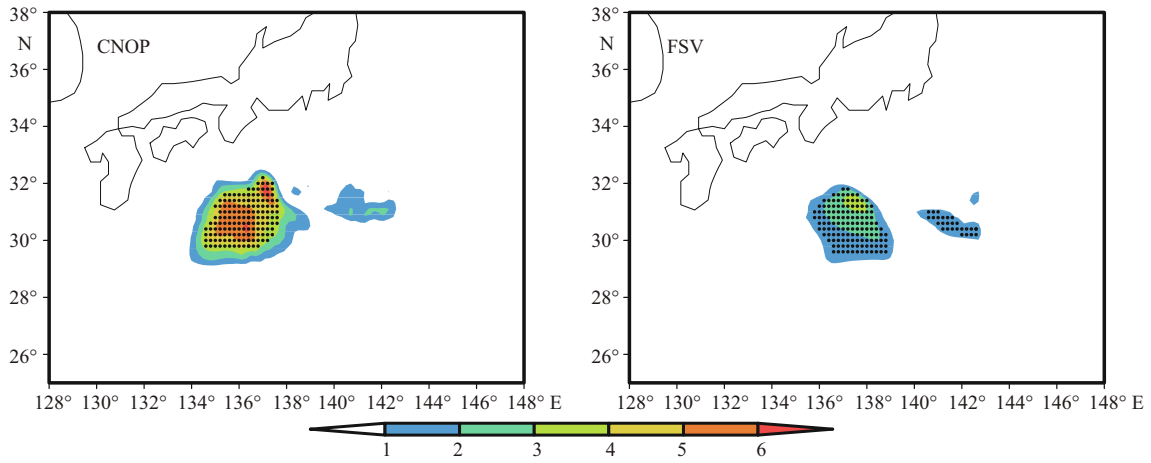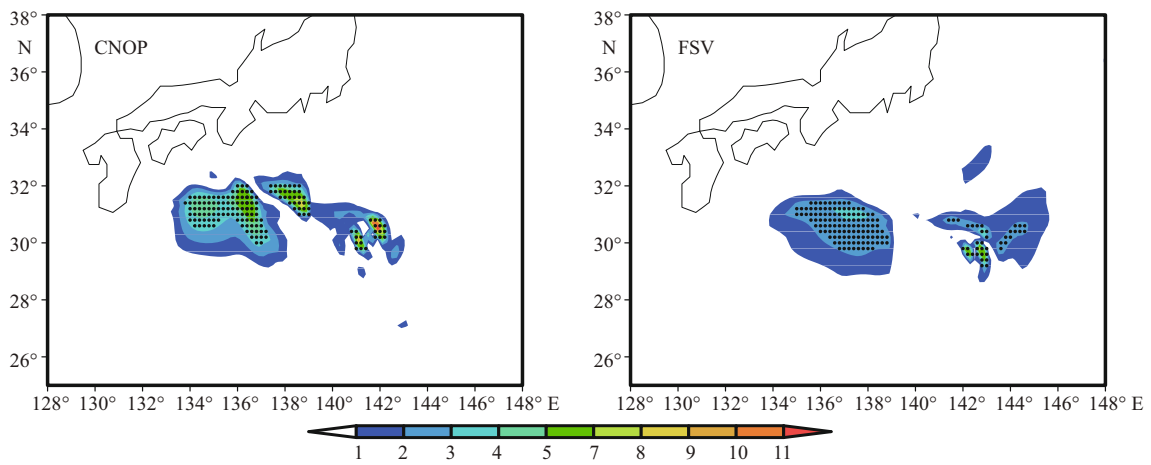Units are m³/s². Regions marked by black solid dots (•) are treated as sensitive areas. The number of grid points is the same as in Cases A and B.
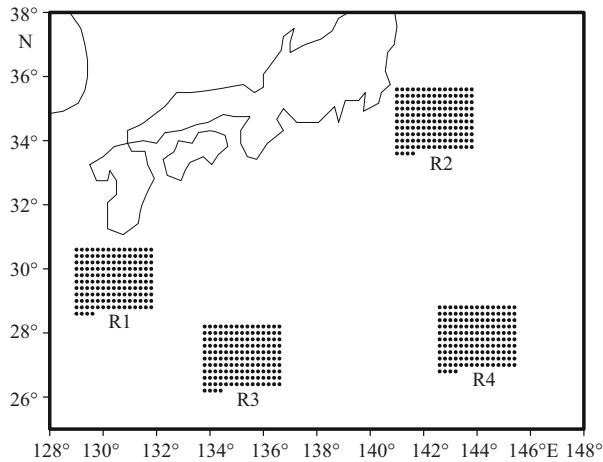
Fig.8 Four randomly selected areas

The numbers of grid points were chosen to be the same as those in sensitive areas in the three cases.

(Usui et al., 2004; Miyazawa et al., 2004, 2008). We therefore investigated whether the two regions are sensitive in the present simple, shallow-water model. However, R1 and R2 were not identified using the method of adaptive observations; for convenience, we regard them as randomly selected.

3.2 Sensitivity experiments

To examine whether the forecast is more sensitive to initial errors in the sensitive areas identified using the CNOP and FSV than to those errors in other areas, we studied the evolution of the errors in different areas. In the first numerical experiment, we superimposed the CNOP- and FSV-type initial errors within the sensitive areas on CNOP-SA, FSV-SA, and four randomly selected areas (R1, R2, R3, and R4) at the target time. We then integrated the model for 240 days. In the second experiment, two types of fields with 40 random initial errors of size $N \times 3$ (N is grid points in sensitive areas and three variables) were generated. Each field of random initial error was produced as follows. Suppose the random sequence of the real number satisfies the normal distribution $N(0, \sigma_{i, j})$, i=1, 2, 3; j=1, 2,…N. A random number is chosen from $N(0, \sigma_{i, j})$ as the random error for variable i at grid point j. We can then obtain a random error field x_r for a region. To compare evolution of the random errors with those of CNOP- and FSV-type errors, the two types of random-error fields x_r are scaled to ensure that their total energy equals that of the CNOP- and FSV-type initial errors within the sensitive areas. The types are respectively designated Ran-type1 and Ran-type2. We chose fields with 40 random initial errors because they not only reflect

Table 1 Kinetic energies of forecast errors caused by CNOP-type, FSV-type, and random-type initial errors for Case A (units: $\times 10^{11}$ m^5/s^2)

Areas	Errors			
	CNOP-type	Ran-type1	FSV-type	Ran-type2
CNOP-SA	49.05	2.56	39.88	1.95
FSV-SA	32.33	1.64	30.82	1.51
R1	6.56	0.55	3.76	0.32
R2	4.73	0.47	2.23	0.20
R3	1.79	0.08	1.01	0.06
R4	2.68	0.14	1.38	0.11

Table 2 Kinetic energies of forecast errors caused by CNOP-type, FSV-type, and random-type initial errors for Case B (units: $\times 10^{11}$ m^5/s^2)

Areas	Errors			
	CNOP-type	Ran-type1	FSV-type	Ran-type2
CNOP-SA	55.65	3.01	33.17	2.04
FSV-SA	32.45	2.06	27.88	1.52
R1	6.67	0.61	4.09	0.36
R2	4.82	0.45	2.74	0.23
R3	1.83	0.12	1.05	0.07
R4	2.51	0.22	1.53	0.14

Table 3 Kinetic energies of forecast errors caused by CNOP-type, FSV-type, and random-type initial errors for Case C (units: $\times 10^{11}$ m^5/s^2)

Areas	Errors			
	CNOP-type	Ran-type1	FSV-type	Ran-type2
CNOP-SA	58.45	3.34	47.49	2.33
FSV-SA	43.66	2.31	38.83	1.87
R1	6.58	0.60	4.20	0.40
R2	4.91	0.48	3.06	0.26
R3	1.85	0.13	1.20	0.09
R4	2.65	0.16	1.87	0.18

random effects but also ensure that the calculations are not too substantial. These random initial error fields were superimposed on the basic state over each corresponding area, and the model was then integrated for 240 days.

The kinetic energy norm in Eq.7 was used to measure evolution of the initial errors. For the three cases, the kinetic energy of forecast errors induced by the CNOP and FSV and average kinetic energy caused by the two types of 40 random initial errors were calculated for each region (Tables 1–3). These tables

Table 4 Benefits (%) achieved by reducing CNOP- and FSV-type initial errors in their corresponding sensitive areas for Case A

C	CNOP	FSV
0.75	38.06%	29.24%
0.50	47.63%	40.31%
0.25	64.77%	55.73%
0.00	78.96%	69.05%

Table 5 Benefits (%) achieved by reducing CNOP- and FSV-type initial errors in their corresponding sensitive areas for Case B

C	CNOP	FSV
0.75	37.90%	32.12%
0.50	48.31%	43.67%
0.25	65.48%	61.65%
0.00	80.36%	78.99%

Table 6 Benefits (%) achieved by reducing CNOP- and FSV-type initial errors in their corresponding sensitive areas for Case C

C	CNOP	FSV
0.75	34.78%	24.95%
0.50	45.56%	33.18%
0.25	58.74%	47.23%
0.00	74.88%	63.57%

illustrate that: (1) the forecast error generated by the CNOP and FSV is larger than that induced by random errors; (2) the average kinetic energy value of forecast errors produced by random errors in sensitive areas is larger than that in randomly selected areas, and the effect of random errors superimposed on the CNOP sensitive areas is greatest; (3) both the CNOP- and FSV-type initial errors in the CNOP sensitive areas strongly impact the final forecasts, with the effect of CNOP-type errors the greatest. In addition, kinetic energies of forecast errors generated by the initial errors superimposed on region R1 are stronger than those for the other randomly selected areas (R2, R3 and R4), indicating that the area of mesoscale fluctuation is also relatively sensitive. These results suggest that the spatial patterns of initial errors and their locations have major effects on the growth of forecast errors. The most likely reason is that the flow is susceptible to barotropic instability (Wang et al., 2013a). Furthermore, sensitive areas determined by the spatial structure of the CNOP are more sensitive than the FSV sensitive regions.

3.3 Idealized hindcasting experiments

In the previous sections, inclusion of the CNOP and FSV resulted in a poorer final prediction. Therefore, eliminating the CNOP-type and FSV-type errors in the initial field appears important. As described in this section, idealized hindcasting experiments were designed to estimate whether the forecast would be improved by reducing the CNOP-type and FSV-type initial errors in the identified sensitive areas.

The forecast error generated by the initial error is defined as

$$J_1(\delta X_0) = \left\| M_t(X_0 + \delta X_0) - M_t(X_0) \right\|_b^2, \tag{11}$$

where δX_0 represents the CNOP or FSV, and M_t, X_0 and $\|\cdot\|_b^2$ are as described for Eq.7.

By reducing initial errors in the sensitive areas, the new forecast error is calculated as

$$J_2(\delta X_0) = \left\| M_t(X_0 + C\delta X_0) - M_t(X_0) \right\|_b^2, \tag{12}$$

where C is a weighting coefficient, taking a value C=1 outside sensitive areas and C=0.75, 0.5, 0.25, 0 inside those areas.

The benefit achieved by reducing the CNOP and FSV is given by the ratio

$$k = \frac{J_1(\delta X_0) - J_2(\delta X_0)}{J_1(\delta X_0)}. \tag{13}$$

Tables 4–6 give results of the ideal hindcasting experiment for the three cases. We found that the predictions were improved by the reductions (or eliminations) of the CNOP- and FSV-type initial errors in their corresponding sensitive areas, and the benefits of reducing the former errors are larger than those of reducing the latter errors in their sensitive areas. These results suggest that forecasts can be improved by identifying sensitive areas using the CNOP method and targeting observations in those areas. Furthermore, adaptive observational networks deployed across the CNOP sensitive areas may have much greater forecast benefits than those across the FSV sensitive areas.

4 DISCUSSION AND CONCLUSION

We used a 1.5-layer shallow-water model to simulate variations in the Kuroshio path. The CNOP and FSV approaches were adopted to identify sensitive areas for adaptive observation in prediction of the Kuroshio LM. For three LM cases, we found

that large amplitudes of both the CNOP and FSV were in the SRG region and south of the Kuroshio extension. When we superimposed the CNOP and FSV on the basic state and integrated the model for 240 days, we found that these two types of initial perturbations strengthened the forecast Kuroshio LM paths. Further, the LM paths induced by the CNOP-type errors were stronger than those induced by FSV-type errors.

The results of sensitivity experiments indicated that the spatial patterns and locations of initial errors greatly affected the growth of forecast errors. Forecast errors generated by the initial errors with CNOP and FSV patterns were larger than those induced by random errors. The effects of random errors introduced into sensitive areas are stronger than those of random errors in the randomly selected areas. Overall, initial errors in the CNOP sensitive areas had greater effects than initial errors in other areas, including the FSV sensitive areas, on the final forecasts. That is, the sensitive areas determined by spatial structures of the CNOP and FSV are indeed sensitive, and the sensitive regions identified by the CNOP method are more sensitive than those identified by the FSV method. Results of an idealized forecast experiment showed the effectiveness of identifying sensitive areas using the two methods, in that predictions were improved by reducing initial errors in those areas. The CNOP-SA was more effective than the FSV-SA. These results suggest that implementing targeted observations in the CNOP-SA would have much greater forecast benefits for prediction of the Kuroshio LM.

The task of identifying sensitive areas in this study was based on the shallow-water model. A high-resolution ocean general circulation model will be considered in future work to examine the usefulness of sensitive areas for adaptive observations obtained using the relatively simple model. When implementing adaptive observation in a real ocean situation for prediction of the Kuroshio LM, the circumstances are more complicated and factors such as observation platforms, the numerical forecast model, and the data assimilation system should be considered. However, we believe that the adaptive observation based on the CNOP method is a useful approach for identifying sensitive areas in the prediction of variations in the Kuroshio path south of Japan.

5 ACKNOWLEDGMENT

References

Baker N L, Daley R. 2000. Observation and background adjoint sensitivity in the adaptive observation-targeting problem. *Quart. J. Roy. Meteor. Soc.*, **126**(565): 1 431-1 454.

Bergot T, Hello G, Joly A, Malardel S. 1999. Adaptive observations: a feasibility study. *Mon. Wea. Rev.*, **127**(5): 743-765.

Berliner L M, Lu Z Q, Snyder C. 1999. Statistical design for adaptive weather observations. *J. Atmos. Sci.*, **56**(15): 2 536-2 552.

Birgin E G, Martínez J M, Raydan M. 2000. Nonmonotone spectral projected gradient methods on convex sets. *SIAM J. Optim.*, **10**(4): 1 196-1 211.

Bishop C H, Etherton B J, Majumdar S J. 2001. Adaptive sampling with the ensemble transform Kalman filter. Part I: theoretical aspects. *Mon. Wea. Rev.*, **129**(3): 420-436.

Bishop C H, Toth Z. 1999. Ensemble transformation and adaptive observations. *J. Atmos. Sci.*, **56**(11): 1 748-1 765.

Buizza R, Montani A. 1999. Targeting observations using singular vectors. *J. Atmos. Sci.*, **56**(17): 2 965-2 985.

Ebuchi N, Hanawa K. 2000. Mesoscale eddies observed by TOLEX-ADCP and TOPEX/POSEIDON altimeter in the Kuroshio recirculation region south of Japan. *J. Oceanogr.*, **56**(1): 43-57.

Ebuchi N, Hanawa K. 2003. Influence of mesoscale eddies on variations of the Kuroshio path south of Japan. *J. Oceanogr.*, **59**(1): 25-36.

Fujii Y, Tsujino H, Usui N, Nakano H, Kamachi M. 2008. Application of singular vector analysis to the Kuroshio large meander. *J. Geophys. Res.*, **113**(C7): C07026, http://dx.doi.org/10.1029/2007JC004476.

Hamill T M, Snyder C. 2002. Using improved background-error covariances from an ensemble kalman filter for adaptive observations. *Mon. Wea. Rev.*, **130**(6): 1 552-1 572.

Hellerman S, Rosenstein M. 1983. Normal monthly wind stress over the world ocean with error estimates. *J. Phys. Oceanogr.*, **13**(7): 1 093-1 104.

Ishikawa Y, Awaji T, Komori N, Toyoda T. 2004. Application of sensitivity analysis using an adjoint model for short-range forecasts of the Kuroshio path south of Japan. *J. Oceanogr.*, **60**(2): 293-301.

Kawabe M. 1995. Variations of current path, velocity, and volume transport of the Kuroshio in relation with the large meander. *J. Phys. Oceanogr.*, **25**(12): 3 103-3 117.

Langland R H, Rohaly G D. 1996. Adjoint-based targeting of observations for FASTEX cyclones. *In*: Proceedings of the Seventh Conference on Mesoscale Processes, Reading. Amer. Meteor. Soc., United Kingdom. p.369-371.

Langland R H. 2005. Issues in targeted observing. *Quart. J. Roy. Meteor. Soc.*, **131**(613): 3 409-3 425.

Majumdar S J, Aberson S D, Bishop C H, Buizza R, Peng M S, Reynolds C A. 2006. A comparison of adaptive observing guidance for Atlantic tropical cyclones. *Mon. Wea. Rev.*, **134**(9): 2 354-2 372.

Mitsudera H, Waseda T, Yoshikawa Y, Taguchi B. 2001. Anticyclonic eddies and Kuroshio meander formation. *Geophys. Res. Lett.*, **28**(10): 2 025-2 028.

Miyazawa Y, Guo X Y, Yamagata T. 2004. Roles of mesoscale eddies in the kuroshio paths. *J. Phys. Oceanogr.*, **34**(10): 2 203-2 222.

Miyazawa Y, Kagimoto T, Guo X Y, Sakuma H. 2008. The Kuroshio large meander formation in 2004 analyzed by an eddy-resolving ocean forecast system. *J. Geophys. Res.*, 113(C10): C10015.

Miyazawa Y, Yamane S, Guo X Y, Yamagata T. 2005. Ensemble forecast of the Kuroshio meandering. *J. Geophys. Res.*, **110**(C10): C10026, http://dx.doi.org/10.1029/2004 JC002426.

Morss R E, Emanuel K A, Snyder C. 2001. Idealized adaptive observation strategies for improving numerical weather prediction. *J. Atmos. Sci.*, **58**(2): 210-232.

Mu M, Duan W S, Wang B. 2003. Conditional nonlinear optimal perturbation and its applications. *Nonlinear Processes in Geophysics*, **10**(6): 493-501.

Mu M, Wang H L, Zhou F F. 2007. A preliminary application of conditional nonlinear optimal perturbation to adaptive observation. *Chin. J. Atmos. Sci.*, **31**(6): 1 102-1 112. (in Chinese)

Mu M, Zhou F F, Wang H L. 2009. A method for identifying the sensitive areas in targeted observations for tropical cyclone prediction: conditional nonlinear optimal perturbation. *Mon. Wea. Rev.*, **137**(5): 1 623-1 639.

Mu M. 2013. Methods, current status, and prospect of targeted observation. *Science China Earth Sciences*, **56**(12): 1 997-2 005.

Palmer T N, Gelaro R, Barkmeijer J, Buizza R. 1998. Singular vectors, metrics, and adaptive observations. *J. Atmos. Sci.*, **55**(4): 633-653.

Pu Z X, Kalnay E, Sela J, Szunyogh I. 1997. Sensitivity of forecast errors to initial conditions with a quasi-inverse linear method. *Mon. Wea. Rev.*, **125**(10): 2 479-2 503.

Pu Z X, Kalnay E. 1999. Targeting observations with the quasi-inverse linear and adjoint NCEP global models: performance during FASTEX. *Quart. J. Roy. Meteor.*

Soc., **125**(561): 3 329-3 337.

Qin X H, Mu M. 2011. A study on the reduction of forecast error variance by three adaptive observation approaches for tropical cyclone prediction. *Mon. Wea. Rev.*, **139**(7): 2 218-2 232.

Qiu B, Miao W F. 2000. Kuroshio path variations south of Japan: bimodality as a self-sustained internal oscillation. *J. Phys. Oceanogr.*, **30**(8): 2 124-2 137.

Taft B A. 1972. Characteristics of the flow of the Kuroshio south of Japan. *In*: Stommel H, Yoshida K eds. Kuroshio: Its Physical Aspects. University of Tokyo Press, Tokyo. p.165-216.

Tsujino H, Usui N, Nakano H. 2006. Dynamics of Kuroshio path variations in a high-resolution general circulation model. *J. Geophys. Res.*, **111**(C11): C11001, http://dx.doi.org/10.1029/2005JC003118.

Usui N, Tsujino H, Nakano H, Fujii Y. 2008. Formation process of the Kuroshio large meander in 2004. *J. Geophys. Res.*, **113**(C8): C08047.

Wang Q, Mu M, Dijkstra H A. 2012. Application of conditional nonlinear optimal perturbation method to the predictability study of the Kuroshio large meander. *Adv. Atmos. Sci.*, **29**(1): 118-134.

Wang Q, Mu M, Dijkstra H A. 2013a. The similarity between optimal precursor and optimally growing initial error in prediction of Kuroshio large meander and its application to targeted observation. *J. Geophys. Res.*, **118**(2): 869-884.

Wang Q, Mu M, Dijkstra H A. 2013b. Effects of nonlinear physical processes on optimal error growth in predictability experiments of the Kuroshio Large Meander. *J. Geophys. Res.*, **118**(12): 6 425-6 436.

Waseda T, Mitsudera H, Taguchi B, Yoshikawa Y. 2003. On the eddy-Kuroshio interaction: meander formation processes. *J. Geophys. Res.*, **108**(C7): 3 220, http://dx.doi.org/10.1029/2002JC001583.

Yu Y S, Mu M, Duan W S, Gong T T. 2012. Contribution of the location and spatial pattern of initial error to uncertainties in El Niño predictions. *J. Geophys. Res.*, **117**(C6): C06018, http://dx.doi.org/10.1029/2011JC007758.